Heliyon 9 (2023) e22027

Contents lists available at ScienceDirect

Heliyon

journal homepage: www.cell.com/heliyon

"Adsorptive removal of Congo Red dye from its aqueous solution by Ag–Cu–CeO_2 nanocomposites: Adsorption kinetics, isotherms, and thermodynamics"

Nitish Semwal [a], Divya Mahar [a], Manjunath Chatti [b], Anirban Dandapat [c], Mahesh Chandra Arya [a,*]

[a] Department of Chemistry, DSB Campus, Kumaun University, Nainital, Uttarakhand, 263002, India
[b] Australian Centre for Electromaterials Science, School of Chemistry, Monash University, Clayton, Victoria, 3800, Australia
[c] Guru Govind Singh Indraprastha University, New Delhi, India

ARTICLE INFO

Keywords:
Ag-Cu-CeO_2
Nanocomposites
Adsorption
Congo red
Pseudo second order
Freundlich isotherm

ABSTRACT

Eliminating synthetic dyes and organic contaminants from water is crucial for safeguarding human health and preserving the environment. In this study, we explored the effectiveness of Ag–Cu–CeO_2 nanocomposites as adsorbents to remove Congo Red dye from water. Three compositions of Ag–Cu–CeO_2 nanocomposites (10:20:70, 15:15:70, and 20:10:70) have been synthesized by the aqueous coprecipitation method. A comprehensive analysis was performed by different techniques including X-ray diffraction, Fourier transform infrared spectroscopy, BET surface area determination, Thermogravimetric analysis, Scanning electron microscopy, and TEM. The synthesized nanocomposites have a dimension of 5 ± 1 nm and a high surface area (51.832–78.361 m^2g^{-1}).

Among these, the nanocomposite with composition 15:15:70 showed the highest adsorption capacity of 4.71 mg/g adsorption (96.83 % removal) from the 0.8 × 10^{-4} M (55.6 mg/l) Congo Red solution at pH values of 2 at 20 °C with contact time of 3h. The adsorption data is best fitted in the Freundlich adsorption isotherm and pseudo-second-order kinetic model. The negative values of enthalpy variation (−27.57, −26.43, and −16.73 kJ/mol) demonstrated that the adsorption was spontaneous and exothermic. The cycling run showed a mere 12 % deactivation after five cycles of use thus indicating that Ag–Cu–CeO_2 nanocomposites hold great potential as effective and eco-friendly adsorbents to remove Congo Red from water.

1. Introduction

The increased demand for synthetic dyes in various industries has led to significant advancements in their production and development over the years [1,2]. The presence of dyes in water ends in a diminution of its quality. Most importantly, the presence of dyes lead to an unsightly appearance and reduction of light that penetrates the water, thus, adversely impacting the photosynthetic activities of aquatic flora [3,4], it lowers the concentration of dissolved oxygen [5]. In addition, their complex structure makes them degradation-resistant, which not only has a detrimental effect on the overall health of the aquatic ecosystem but also poses risk to

* Corresponding author.
E-mail address: mcarya181@gmail.com (M. Chandra Arya).

https://doi.org/10.1016/j.heliyon.2023.e22027
Received 8 July 2023; Received in revised form 2 November 2023; Accepted 2 November 2023
Available online 7 November 2023

human health due to their toxicity and carcinogenicity [6,7].

Congo Red (CR) is one of the highly soluble and stable anionic diazo dyes used in various industries such as textile, plastic, cosmetics, and pharmaceutical [8]. As a reactive azo dye with an azo group (N]N) in its structure, CR is not biodegradable [9]. Metabolizing CR produces benzidine, which can cause hazardous effects on human health, including gastrointestinal, eye, and skin irritation, blood clotting, somnolence, and breathing problems [10]. Therefore, it is crucial to eliminate CR from the effluent before discharging it into the aquatic system to prevent plausible harm to the environment and human health.

Nanocomposites have been explored as adsorbents to remove various dyes from effluents. For example, CeO_2-containing adsorbents, including chitosan-based nanocomposites [11], Fe_3O_4/CeO_2 [12], and Zn/CeO_2-NC [13], have found their application in dye removal due to their high efficiency, regeneracy, and heterogeneity. Also, the Ag-doped nanocomposites showed enhanced efficiency towards dye removal from wastewater due to the incorporation of Ag atoms at the surface of nanocomposites and their interaction with matrix and the functional groups on the surface [14]. However, most of the previous studies focused on exploitation of photocatalytic potential of ZnO, TiO_2, CeO_2 -based nanocomposites and its enhancement by doping Ag. The Ag-doped nanocomposites have been underexplored for their adsorption potential and that too, limited to their use for adsorptive removal of certain ions only viz. viz. Hg^{2+}, Cr (VI), and fluoride ions [15,16]. [17–19]. Moreover, the high percentage (25–50 %) of Ag- in these Ag-doped nanocomposites makes them costly and economically nonviable. A scant literature is available on the adsorption potential of Ag-mixed metal doped metal oxides. Herein, we have focused on investigating the influence of bimetallic doping, specifically Ag with Cu, on the adsorption capabilities of cerium oxide so as to reduce the percentage of Ag by replacing it with Cu and at the same time getting optimum adsorption efficiency of doped CeO_2 nanocomposite. Cu has been chosen as the substitute of Ag because both are group 11 metals and have similarities. Three different compositions of Ag–Cu–CeO_2 nanocomposites have been synthesized using a simple aqueous co-precipitation method. These have been characterized by using different microscopic techniques and XRD, and BET analyses. The synthesized bimetallic nanocomposites have been studied for their adsorption potential towards the aqueous solution of CR dye. The key parameters have been optimized and to gain a comprehensive understanding of the adsorption process, we employed kinetic and equilibrium adsorption isotherm models for data analysis. Our results demonstrated that the Ag–Cu– CeO_2 nanocomposites were highly effective in the adsorptive dye removal.

2. Materials and methods

The analytical grade reagents were obtained from Sigma Aldrich including silver acetate, 98 % (CH_3COOAg), cerium nitrate hexahydrate, 99.9 % (Ce $(NO_3)_3{\cdot}6H_2O$), copper sulphate, 99.5 % ($CuSO_4$), Congo Red (MW: 696.66; g/mol λ_{max} = 498 nm) ($C_{32}H_{22}N_6Na_2O_6S_2$), cetyltrimethylammonium bromide, 99 % (CTAB). These reagents were utilized in their as-received form without any modifications. Deionized water was used for solution preparation and washing processes.

2.1. Synthesis of Ag–Cu–CeO_2 nanocomposites

The aqueous co-precipitation method was employed for the synthesis of the nanocomposites (Fig. 1). Initially, 100 mL of aqueous

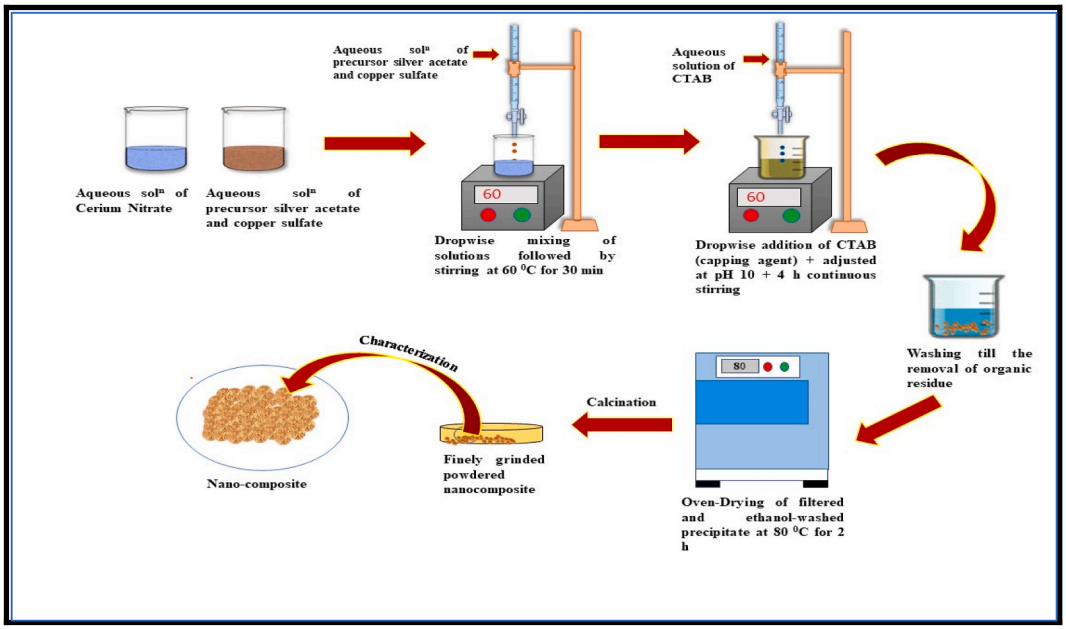

Fig. 1. Schematic diagram of the synthesis process of Ag–Cu–CeO_2 nanocomposites.

solutions of desired concentrations of silver acetate and copper sulphate were mixed together to form an aqueous solution of metal precursors. It was mixed dropwise with an aqueous solution of cerium nitrate hexahydrate of the desired concentration with the aid of a burette while continuously stirring the mixture at 500 rpm for 30 min at 60 °C. Subsequently, CTAB solution was gradually added dropwise to the above mixture and the entire solution pH was maintained at 10 using NaOH. The solution was stirred for another 4 h at 60 °C to ensure a complete reaction and formation of the precipitate. The precipitate was filtered and washed multiple times with deionized water followed by ethanol washing to ensure the impurities removal. The washings were checked repeatedly for the presence of sulphate, acetate, and nitrate ions. The moisture was subsequently removed from the precipitate by drying it for 2 h at 80 °C. Finally, to enhance crystallinity and get rid of any remaining organic components, the powder was annealed in a furnace for 4 h at 600 °C. After that, a mortar and pestle were used to grind the annealed material into a fine powder suitable for further investigation. The following three different compositions of the Ag–Cu–CeO_2 nanocomposites were synthesized for the study:

1. 10 % Ag, 20 % Cu, and 70 % CeO_2 by weight denoted as ACC 10:20:70.
2. 15 % Ag, 15 % Cu, and 70 % CeO_2 by weight denoted as ACC 15:15:70.
3. 20 % Ag, 10 % Cu, and 70 % CeO_2 by weight denoted as ACC 20:10:70.

2.2. Characterization techniques

The crystallographic analysis of the nanocomposites was conducted using a Bruker D8-Advance P-X ray diffractometer, set to a current of 40 mA, with a 30 kV accelerating voltage and a wavelength (λ) of 1.5405 Å Cu-Kα radiation. To ascertain the nanocomposites' crystal structure, the diffraction data were gathered over a 2θ range of 10°-90°. SEM analysis was conducted using an instrument at 10 kV, employing different scan rates. The samples were dispersed in ethanol and drop-cast onto a silicon wafer for analysis. TEM analysis was performed on FEI Tecnai G2 F30S at 300 kV. Surface area and pore size investigations were performed using the Quantachrome® ASiQwin™-Automated Gas Sorption instrument. Additionally, FT-IR analysis of the nanocomposites was carried out using a PerkinElmer spectrum instrument. which enables the identification of functional groups and the analysis of chemical bonds in a material. Thermogravimetric analysis was also performed by PerkinElmer.

2.3. Adsorption experiment

The adsorption potential of the synthesized nanocomposites was investigated by batch adsorption studies by taking a standard solution of 55.6 mg/l (0.8×10^{-4} M) of CR natural pH of this solution was measured to 8.2.100 mg of the nanocomposites was added to a 100 mL solution of CR in an Al-foil-covered beaker. Continuous stirring was performed at 500 rpm throughout the experiment using a magnetic stirrer to ensure proper dispersal of the nanocomposite. At every 30-min interval, 5 mL of the solution was pipette out and centrifuged at 5000 rpm to get the aliquot. A calibrated Systronics double-beam UV–visible spectrophotometer was used to quantify the leftover dye concentration in the aliquot by spectrophotometry. The Adsorption efficiency of nanocomposites towards CR was calculated using equation (1):

$$\frac{C}{C_0} = \frac{(C_o - C_e)}{C_o} \tag{1}$$

here $\frac{C}{C0}$ represents the adsorption efficiency, C_0 is the initial concentration of CR solution (mg l^{-1}), and Ce is the CR aliquot's final concentration (mg l^{-1}):

$$q_e = \frac{V}{m}(C_o - C_e) \tag{2}$$

Equation (2) was used to calculate the amount of CR adsorbed at equilibrium (q_e, mg/g) by each adsorbent, where volume of CR solution is denoted by V, and adsorbent mass is denoted as m.

The optimization of the following parameters in the range given below was also performed in this study:

1. pH (2–12)
2. Dosage of nanocomposite (0.01–0.05 g)
3. Contact time (0–180 min)
4. CR concentration (13.6–55.6 mg/L),
5. Temperature (10–60 °C)

The typical leaching experiments were also performed to retrieve the adsorbent from the reaction mixture which was washed multiple times with double distilled water, organic solvents with sulphuric acid and then dried for 2 h in hot air oven at 100 °C. The adsorbent thus obtained was reused to assess its recyclability.

2.4. Adsorption isotherm

Adsorption isotherm study was done by analysing the adsorption data using Langmuir, Freundlich, and D–R

(Dubinin–Radushkevich) isotherms.

The Langmuir isotherm is based on the concept of dynamic equilibrium between adsorption and desorption rates. It considers that the amount of adsorbate adsorbed is proportional to the portion of the available adsorbent surface that is used for adsorption, while the amount of adsorbate desorbed is related linearly to the fraction of the surface that is already covered. In other words, adsorption occurs when there are empty sites available for adsorption, while desorption occurs when all sites are occupied.

Langmuir adsorption can be expressed in equation (3):

$$\frac{C_e}{q_e} = \frac{1}{q_m K_L} + \frac{C_e}{q_m} \tag{3}$$

where the equilibrium concentration of the adsorbate (Ce) is related to the adsorption capacity of the adsorbent (q_m) through the Langmuir constant (K_L). The Langmuir constant is a parameter that characterizes the adsorption capability of an adsorbent, and it is influenced by the porosity and surface area of the material. High surface area and high pore volume of the adsorbent increases the capacity to adsorption [20]. This implies that there is a close relationship between the adsorbent's physical characteristics and the Langmuir constant, and it can be used to compare the effectiveness of different materials for a particular adsorption process.

A model for describing the adsorption behaviour of molecules on surfaces is the Freundlich isotherm. which assumes that multi-layer adsorption occurs and that there is an exponential decay in the distribution of energies of the adsorbed sites [21].

The Freundlich isotherm is expressed by equation (4):

$$log\ q_e = log\ K_F + \frac{1}{n} log\ C_e \tag{4}$$

where K_F represents the capacity of adsorption (l/mg) and $\frac{1}{n}$ represents the intensity of adsorption, which reflects the degree of heterogeneity of the adsorbent surface and the distribution of active sites with varying adsorption energies.

The D–R (Dubinin–Radushkevich) isotherm is a mathematical model applied to describe the condition of physical or chemical adsorption.

D–R activity coefficient B in mol^2/kJ^2 and adsorption capacity Q_m in mg/g, were calculated from equation (5):

$$ln\ q_e = ln\ Q_m - B\varepsilon^2 \tag{5}$$

Polanyi potential ε in kJ/mol is calculated from equation (6):

$$\varepsilon = RT\ ln + \left(1 + \frac{1}{C_e}\right) \tag{6}$$

The mean energy of the adsorption process in kJ mol^{-1} is calculated by equation (7):

$$E = \frac{1}{\sqrt{2B}} \tag{7}$$

2.5. Thermodynamics studies

To investigate the behavior of CR adsorption onto Ag–Cu–CeO_2 nanocomposites, thermodynamic variable like the Gibbs free energy change (ΔG°), entropy change (ΔS°), and enthalpy change (ΔH°) were calculated. The experiments were performed over a range of temperature between 10 and 60 °C (283–333 K). The ΔG° values were calculated using equation (8):

$$\Delta G^o = -RT\ lnK \tag{8}$$

The values of ΔH° and ΔS° were obtained by plotting lnK against 1/T and using Van't Hoff's as equation (9):

$$lnK = \frac{\Delta S^o}{R} - \frac{\Delta H^o}{T}\ \left(\frac{1}{T}\right) \tag{9}$$

where ΔS_o is the standard entropy change.

2.6. Kinetic studies

The investigation of kinetics of adsorption is a valuable approach to gaining a more comprehensive understanding of the adsorption mechanism and determining crucial kinetic parameters such as rate constants, that are crucial for future industrial applications [22]. The primary focus of this experiment was to examine the kinetics of CR adsorption by measuring the equilibrium adsorbate concentration (q_e) over a period of time.

The Lagergren pseudo-first-order equation (equation (10)) [23] and the Ho pseudo-second-order equation (equation (11)) [24] are two widely used rate equations that are frequently used in adsorption investigations to calculate the rate of adsorption. These equations offer crucial insights into the adsorption process and can aid in identifying the best industrial application conditions.

$$log(q_e - q_t) = log(q_e) - \left(\frac{k_1}{2.303}\right)t \tag{10}$$

$$\frac{q}{t} = \frac{1}{k_2 q_e^2} + \frac{t}{q_e} \tag{11}$$

Here, measured the quantity of adsorbent used (W, measured in grams) and tracked the adsorption capacities at equilibrium and over time (qe and qt, respectively, measured in milligrams per gram). Furthermore, we determined the rate constants (k_1 and k_2, respectively) for the pseudo-first-order and pseudo-second-order adsorption processes.

3. Result and discussion

3.1. Powder X-ray diffraction analysis of Ag–Cu–CeO_2 (ACC) nanocomposites

The XRD analysis was utilized to determine the type of the produced crystalline phases and to compute crystallite size using Scherrer's equation. The X-ray diffraction pattern for the as-produced Ag–Cu–CeO_2 (ACC) nanocomposites of various compositions showed the typical peaks at 28.6, 33.1, 47.5, and 56.4°, which, respectively, correspond to the CeO_2 reflection planes (111), (200), (220), and (331) and are in agreement with the standard pattern of CeO_2 (JCPDS card No. 34–0394). The calculated average crystallite size (D) of differently doped and bare CeO_2 ranges between 6 and 7 nm.

Debye-Scherrer formula (equation (12)) was applied to evaluate the crystallite size of the synthesized ACC NCs:

$$crystallite\ size\ (\varphi) = \frac{0.94\lambda}{\beta\ cos\ \theta} \tag{12}$$

where, β represents the full-width at half-maximum (FWHM) of the XRD diffraction peak of highest intensity, while θ denotes the corresponding Bragg diffraction angle. The X-ray source used had a wavelength of 0.1504 nm, and the constant of 0.94 is known as the shape factor. These results have been summarised in Table 1:

The lattice parameter values, calculated by using the free software MAUD- Materials Analysis Using Diffraction, showed a slight variation from the pure CeO_2 phase (5.411 Å), which can be attributed to the incorporation of Ag and Cu ions into the CeO_2 lattice.

However, it is interesting to observe that the Ag/Cu-containing catalysts exhibit the reflections that are typical of metallic Ag/Cu particles. Peaks at 43.5° (111) and 73.90° (220) in Fig. 2(a) and (b) indicate the presence of Cu metal in the CeO_2 lattice (JCPDS No. 85–1326) [25] Also, a peak at 30.98° corresponds to Cu_2O with some shifting in values [26,27] These XRD data proves the presence of Cu in metallic as well as in the oxidised form in the nanocomposites. The peaks at 2θ values of 38.14°, 64.38° and 77.21° in Fig. 2(c) correspond to the (111), (220), and (311) planes of face-centered cubic (fcc) crystalline silver (Ag), respectively (JCPDS files no. 03–0921) [28], [29]. These observations distinctly prove that apart from lattice incorporation, the secondary metals also coexist in the form of individual metallic oxides and metals leading to formation of the multiphase system and the effective deposition of Ag and Cu metals on the CeO_2 surface within the nanocomposite.

3.2. SEM analysis

The SEM images of ACC nanocomposites with composition ratios 10:20:70, 15:15:70 and 20:10:70 have been shown in Fig. 3(a–c), The images depict the distinctive spherical morphology exhibited by all three compositions of ACC nanocomposites, showcasing a certain level of agglomeration. The average particle size was observed to be in the micrometer range. This agglomeration behavior can be ascribed to the inherent high surface energy possessed by the synthesized particles, which drives their propensity to cluster and form larger agglomerates.

3.3. TEM analysis

The nanocomposite with composition 15:15:70 (ACC 15:15:70) was opted for TEM analysis as it showed the best adsorption results. The TEM analysis was carried out at two different scales, 20 nm and 5 nm, to gain insights into its structural characteristics and particle size distribution. When viewed at a 20 nm scale, the ACC 15:15:70 nanocomposite exhibits a remarkable degree of uniformity and spherical morphology (Fig. 4(a)). The nanoparticles appear to be well-defined and consistently sized, indicating a high degree of precision in the synthesis process. Despite the reduced scale at 5 nm (Fig. 4(b)), the nanoparticles continue to maintain their spherical shape, affirming the consistency of the synthesis method. Additionally, Fig. 4(c) and (d) represent particle size distribution curves at

Table 1
XRD Characteristics of Ag–Cu–CeO_2 nanocomposites.

Sample	Peak position (°)	FWHM (^{0})	Lattice parameter (Å)	Crystallite size (nm)
ACC 10:20:70	28.74	1.33216	5.687	6.80
ACC 15:15:70	28.65	1.31121	5.665	6.87
ACC 20:10:70	28.65	1.50217	5.665	6.00

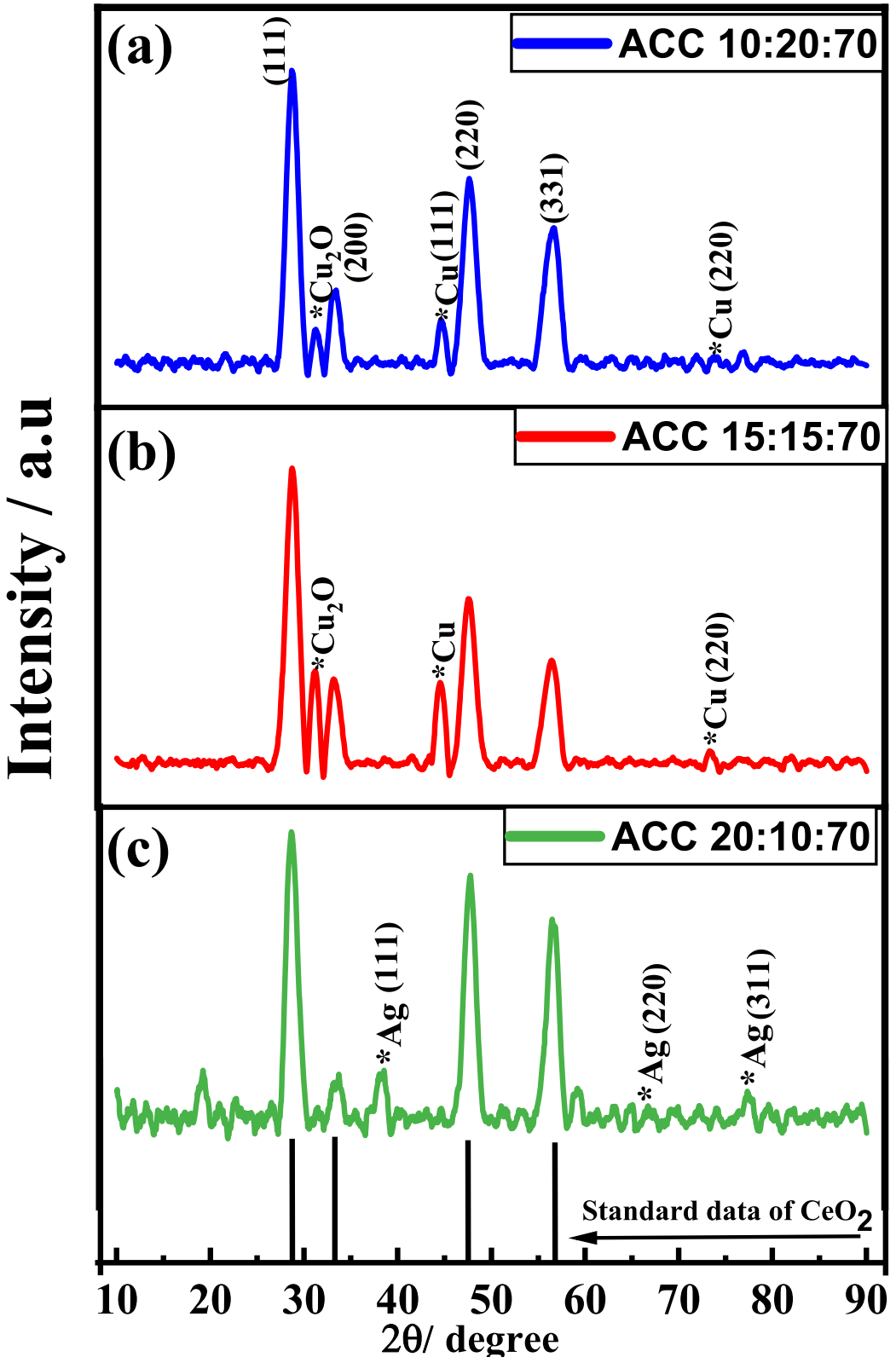

Fig. 2. XRD Spectra of (a) ACC 10:20:70 (b) ACC 15:15:70 (c) ACC 20:10:70 nanocomposite.

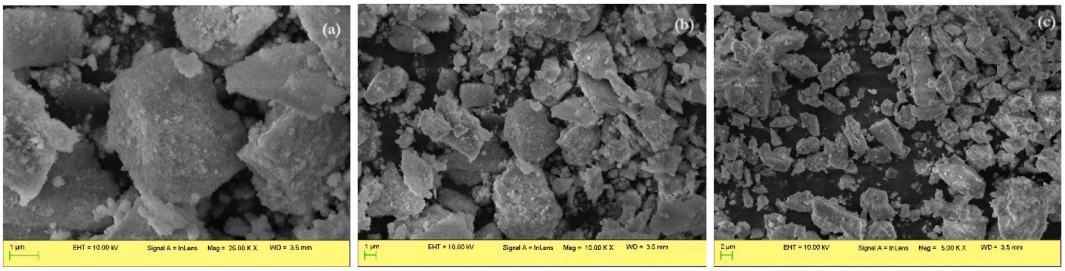

Fig. 3. SEM images of (a) ACC 10:20:70, (b) ACC 15:15:70, (c) ACC 20:10:70 nanocomposites.

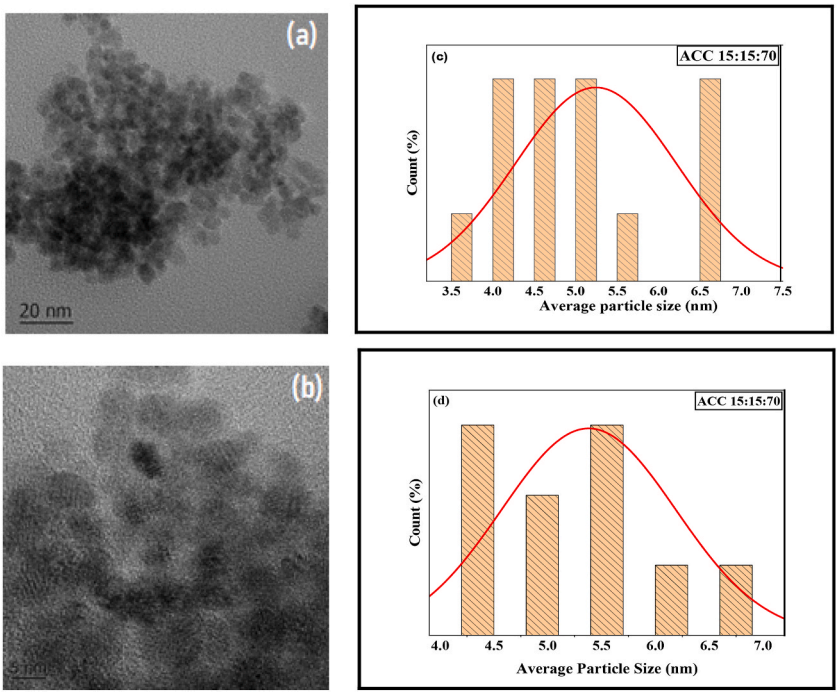

Fig. 4. TEM images of (a) ACC 15: 15:70 (20 nm), (b) At high resolution (5 nm) and particle size distribution curve (c) ACC 15:15:70 at 20 nm scale and (d) ACC 15:15:70 at 5 nm scale.

20 nm and 5 nm scales, respectively. The mean particle size formulated from these curves comes to be 5.2435 nm for 20 nm scale while 5.3806 nm is for 5 nm scale. These consistent morphology and size uniformity are indicative of the high-quality production of these nanocomposites, making them suitable for adsorption phenomenon.

3.4. FT-IR analysis

FT-IR analysis of all three nanocomposites: ACC (10:20:70), ACC (15:15:70), and ACC (20:10:70) were carried out before and after the adsorption experiments. The changes in the FT-IR peaks of the nanocomposites after adsorption suggest the interaction of the nanocomposites with the adsorbate. The FT-IR spectra of ACC (10:20:70) nanocomposite before and after adsorption are shown in Fig. 5 (i) (a) and Fig. 5 (i) (b). The FTIR spectrum of ACC 10:20:70 nanocomposite before adsorption showed peaks at 504.01 cm^{-1} (stretching of Ce–O bond) [30], 1106.93 cm^{-1} (stretching of Cu–O bond), 1631.55 cm^{-1} (O–H bending mode of associated water) [31], and 3300.25 cm^{-1} (O–H bond stretching of associated water) [32]. The dye adsorption caused some existing peaks to vanish and new peaks to emerge. After the adsorption, the new peaks appeared mainly to correspond to different structural units/groups of the adsorbed dye CR. For example, the peak at 1258.85 cm^{-1} is attributed to the C–N stretching vibration of the azo group in CR, whereas the peak at 1016 cm^{-1} is assigned to the benzene ring's C]C stretching vibration. The peak at 796 cm^{-1} is due to the C–H bending vibration of the benzene ring. The peak at 1631.55 cm^{-1} disappeared, indicating CR adsorption and the peak at 504.01 cm^{-1} shifted to

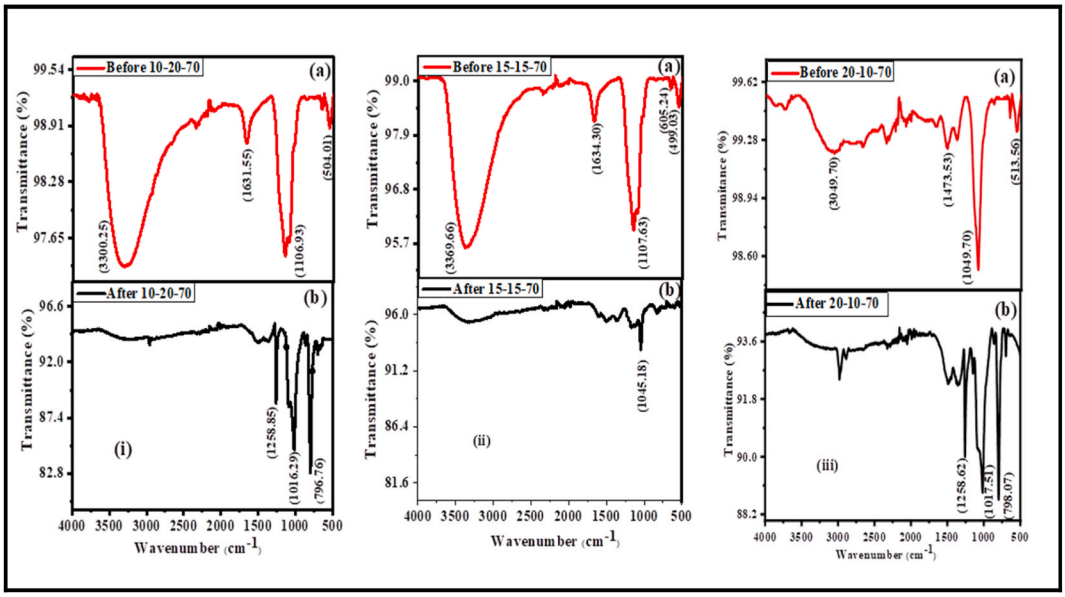

Fig. 5. FT-IR Graph of (i) ACC 10:20:70 nanocomposite (a) before adsorption (b) After adsorption (ii) ACC 15:15:70 nanocomposite (a) before adsorption (b) After adsorption (iii) ACC 20:10:70 nanocomposite (a) before adsorption (b) After adsorption.

a lower frequency, confirming the interaction with CR [33]. The disappearance of the peak at 3300.25 cm^{-1} also indicates involvement of hydroxyl groups in adsorption.

The Changes occur in FTIR spectra of ACC 15:15:70 and ACC 20:10:70 before and after adsorption was shown in Table 2 for ready reference.

The absence of other peaks after adsorption for ACC (15:15:70) suggests minimal alteration to the nanocomposite structure.

In conclusion, the changes in FTIR peaks before and after adsorption indicate the interaction of the nanocomposites with the adsorbate, which can be attributed to the formation of new chemical bonds or hydrogen bonding.

3.5. BET analysis

The results regarding the total surface area, total pore volume, and average pore diameter of ACC nanocomposites at different compositions obtained by the BET analysis are tabulated in Table 3.

The total surface area is obtained to be 78.361 m^2/g, 55.092 m^2/g, and 51.2 m^2/g for ACC (10:20:70), ACC (15:15:70), and ACC (20:10:70) nanocomposites respectively. It is evident from Table 3 that when the concentration of Ag increased, the overall surface

Table 2
FTIR data of ACC (15:15:70) and ACC (20:10:70).

Composition	Peak at (Before Adsorption) (cm^{-1})	Peak of (Before adsorption)	Reference	Peak at (After Adsorption) (cm^{-1})	Peak of (After adsorption)	References
ACC (15:15:70) Fig. 5(ii) **(a-b)**	499.03	Ce–O bond	[34]	1045.18 (C–O bond)	C–O bond	[35]
	605.24	Stretching vibration of Ce–O bond	[34]			
	1107.63	Cu–O bond				
	1634.30	O–H bending mode of associated water	[31]			
	3369.66	O–H bond	[36]			
ACC (20:10:70) Fig. 5(iii) (a-b)	513.56	stretching vibration of Ce–O bond	[37]	1258.62	C–N bond	[38]
	1049.70	stretching vibration of Ag–O bond	[39]	1017.51	Hydrogen bonding (N–H bond	[40]
	1473.53	bending vibration of O–H bond	[41]	798.07	C–H bond	[40]
	3049.70	stretching vibration of C–H bond	[41]			

Table 3
BET Characteristics of Ag–Cu–CeO_2 nanocomposites.

Samples	S_{BET} (m^2/g)	Average pore diameter(nm)	Total pore volume(cm^3/g)
ACC 10:20:70	78.361	5.562	0.194
ACC 15:15:70	55.092	4.867	0.197
ACC 20:10:70	51.832	9.490	0.123

area dropped. This decrease is possibly due to the formation of larger particles or a decrease in exposed surface area [42]. The ACC (15:15:70) nanocomposite has the highest total pore volume despite having a lower surface area, suggesting that the presence of Cu and CeO_2 contributes to a more porous structure. The ACC (20:10:70) nanocomposite has the largest average pore diameter, possibly due to the presence of larger Ag particles [43].

The N_2 adsorption-desorption curve shown in Fig. 6 indicates that the nanocomposites ACC 10:20:70 and ACC 15:15:70 exhibit isotherm type IV Characteristics, this adsorption pattern exhibits a distinctive trend with a sharp and swift increase in adsorption observed at lower relative pressures [44]). As the relative pressure continues to increase, the rate of adsorption gradually slows down, resulting in a more gradual and incremental increase in adsorption. This behavior is commonly observed in materials having mesoporous structures, where the distribution of pore sizes is centered around a certain pore diameter [45]. On the other hand, the material ACC 20:10:70 exhibits isotherm type V behavior, which suggests that the weak adsorbent-adsorbate interactions are responsible for the observed adsorption behavior [46].

3.6. TGA analysis

Thermogravimetric analysis was performed on the nanocomposites to evaluate their thermal stability and phase transitions. The analysis was conducted across a temperature range of 30 °C–750 °C. in the TGA of the synthesized material is shown in Fig. 7 (a). It was observed that a marked weight loss was evident between 50 °C and 200 °C, potentially attributable to the evaporation of adsorbed water molecules and organic residue. The graph revealed minimal weight loss between 250 °C and 750 °C, indicating the absence of any breakdown of the nanocomposites' structure or phase transitions. So, the stability of nanocomposites up to 750 °C suggests their potential in high-temperature applications as adsorbent.

The TGA of used adsorbent, ACC 15:15:70, after desorption, (Fig. 7(b)), illustrates the extent of weight loss following the adsorption process. It reveals that even after undergoing adsorption, the nanocomposite remains stable at elevated temperatures.

4. Optimizing adsorption parameters

Before conducting the adsorption experiment, the concentration range of CR was ascertained in which it followed Lambert's Beer Law. A calibration curve was plotted to ensure that the linear regression coefficient value was close to one for optimal results. Here are the results of the optimization of various parameters:

4.1. Influence of pH

The pH value of a dye has an impact on its adsorption capacity, by adjusting the pH of the dye solution in the range of 2–12, the impact of pH on adsorption effectiveness has been investigated and depicted in Fig. 8. 0.1 M solutions of HCl and NaOH were used to adjust the pH of the dye solution. The research on CR dye revealed that as the pH of the dye solution was reduced from 8 to 2, the

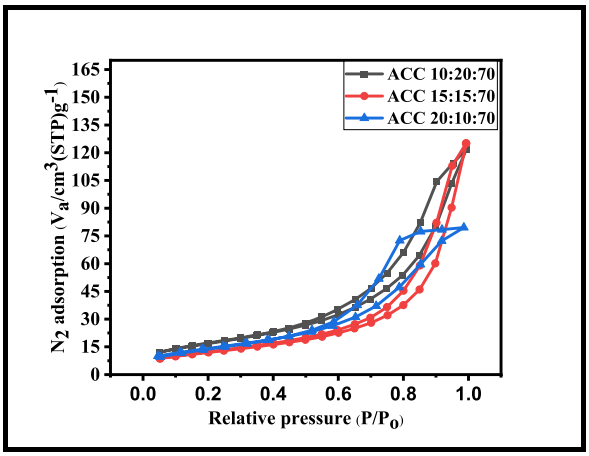

Fig. 6. N_2 adsorption–desorption isotherms of Ag–Cu–CeO_2 nanocomposites.

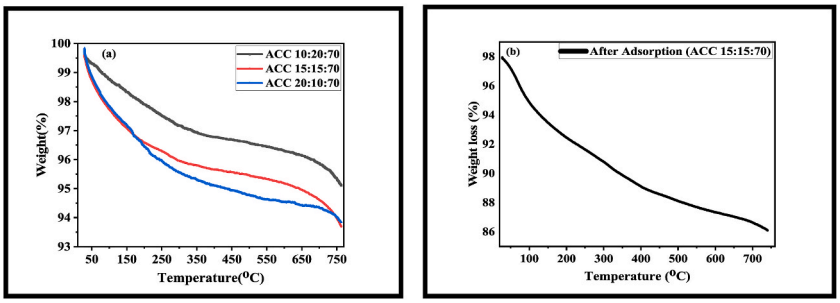

Fig. 7. Thermogravimetric analysis (a) Before Adsorption (b) After Adsorption (ACC 15:15:70).

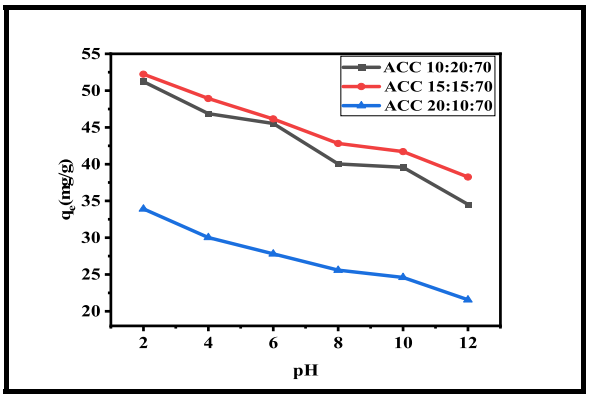

Fig. 8. Influence of pH on Congo Red dye removal. (Temperature - 20 °C, C_o - 55.6 mgl^{-1}, m - 0.1 g, and Time- 180 min).

effectiveness of adsorbents increased. The dye removal rate was highest at pH 2, but as the pH rose from 8 to 12, the dye removal rate was substantially decreased.

Based on the catalyst's surface charge characteristics, it is possible to explain the dye removal rate's apparent dependence on dye solution pH [47]. The catalyst's surface is positively charged at pH levels that are acidic. An anionic dye like CR interacts favourably with the catalyst's surface, which leads to a high extent of dye degradation. On the other hand, the catalyst surface becomes negatively charged at alkaline pH levels. As a consequence, the dye molecules interact negatively with the catalyst's surface, slowing the rate of dye breakdown [48].

4.2. *Influence of adsorbent dose*

The amount of adsorbent influences the adsorbent's removal capacity under specific conditions, which is a critical factor in the

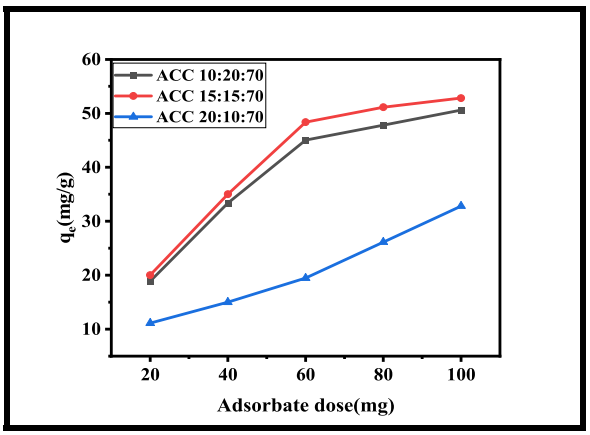

Fig. 9. Influence of the amount of adsorbate on Congo Red dye removal. (Temperature - 20 °C, C_o - 55.6 mgl^{-1}, pH-2, and Time- 180 min).

adsorption process. To assess the consequences of the adsorbent dose, nanocomposites with doses ranging between 0.02 and 0.1 g per 100 mL of CR dye solution were used under optimized conditions of pH, 55.6 mg/l dye solution, 400 rpm shaker speed, and 20 °C temperature. The results, as depicted in Fig. 9, indicate that as the adsorbent dose rose from 0.02 to 0.1 g per 100 mL of dye solution, the nanocomposites' adsorption capability increased. As the amount of adsorbent used increases, there is a corresponding increase in the adsorption of CR. This can be explained by the fact that a greater quantity of adsorbent creates more surface area for the CR molecules to bind to, and also increases the number of available active sites for adsorption [49].

4.3. Influence of contact time

The adsorption efficiency of Ag–Cu–CeO_2 nanocomposites towards CR was studied with varying contact times. The results of the batch experiment suggest that initially, the CR adsorption was very fast, but it gradually slowed down, eventually reaching equilibrium. The graph is displayed in Fig. 10 shows a decreasing trend in the rate of adsorption over time, with the highest removal efficiency occurring at the start of the process when on the surface of the adsorbent there were still many empty binding sites. As the binding sites became occupied, the adsorbent capacity of adsorption approached equilibrium since no more binding sites were available [50]. The adsorption reaction was observed to be very fast within the first 60 min, after which it slowed down, and the adsorption value very slowly increased up until 150 min. No further change in the adsorption value was observed after 180 min. At the equilibrium contact time, the nanocomposite exhibited adsorption capacities of 54.15, 54.54, and 33.91 mg/g for ACC 10:20:70, ACC 15:15:70, and ACC 20:10:70 respectively.

4.4. Influence of concentration

The dye's initial concentration ranges between 13.6 mg/l to 55.6 mg/l while maintaining a constant amount of 0.1g of adsorbent at 20 °C and pH 2. The results revealed that the nanocomposites adsorption efficiency consistently increased upon increasing the concentration of dye in the solution (Fig. 11). It was observed that the ACC 15:15:70 nanocomposite exhibited the highest removal efficiency at lower concentrations of the dye (13.6 mg/l) because the saturation of the adsorption sites on the adsorbent surface brought on by an increment in the initial dye concentration in the solution would eventually result in a reduction in the removal effectiveness [51].

4.5. Influence of temperature

The influence of temperature on CR adsorption on nanocomposites was studied at the temperature from 10 °C to 60 °C (Fig. 12). The outcomes suggest that the CR adsorption on the nanocomposites decreases linearly with the increase in the temperature of adsorption. The study showed that the removal of CR was favoured by low temperatures. This is attributed to the involvement of poor interaction forces during the process of adsorption. A rise in temperature weakens these adsorptive forces, leading to a breakdown and ultimately resulting in a decrease in CR removal at higher temperatures [52].

5. Adsorption isotherm

Experimental data analysis for the adsorption isotherm by employing the Langmuir, Freundlich, and D-R models is presented in Fig. 13(a) and (b), and 13(c), respectively, for all nanocomposites. Table 4 represents the isotherm factors which were calculated from the values of the intercepts and slopes obtained from these curves. The values in the table indicate that ACC composition with a ratio of 15:15:70 exhibits the highest adsorption capacity (q_{max}) among the three compositions, with a value of 78.12. Additionally, it has a relatively high Langmuir constant value (K_L) of 0.277, which suggests a strong affinity between this ACC composition and the

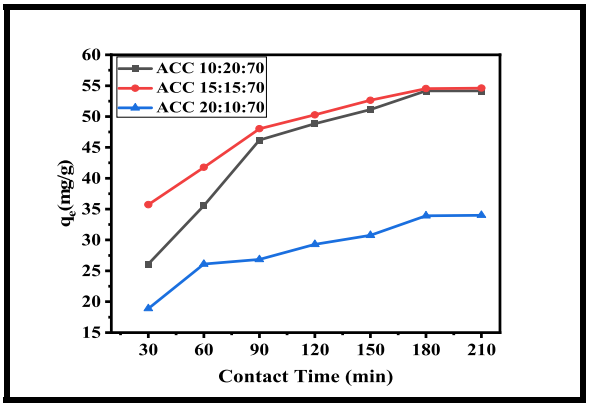

Fig. 10. Influence of contact time on Congo Red dye removal. (Temperature - 20 °C, C_o - 55.6 mgl^{-1}, pH-2, and m- 0.1 g).

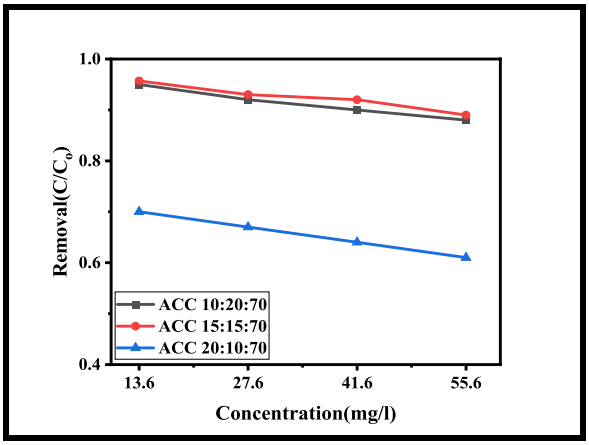

Fig. 11. Influence of concentration on Congo Red removal. (Temperature - 20 °C, pH-2, m- 0.1 g and Time - 180min).

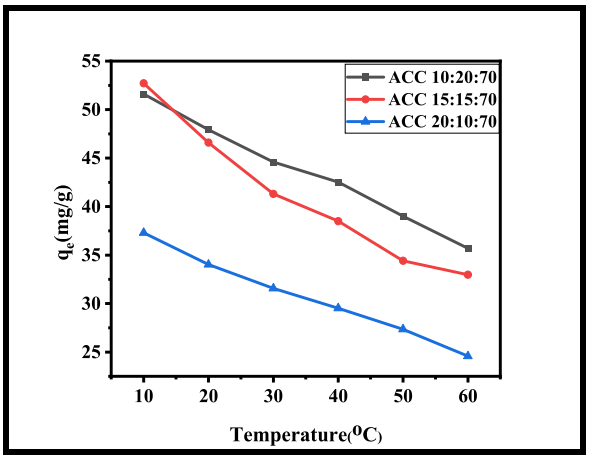

Fig. 12. Influence of temperature on Congo Red removal. (C_o - 55.6 mgl^{-1}, pH-2, m- 0.1 g and Time - 180min).

adsorbate. Among the three models compared (Langmuir, Freundlich, and D-R model), the Freundlich model exhibited the highest R^2 value, indicating that the empirical data of this adsorption are better fit by this model [53] This suggests that the adsorption process involves both monolayer and multilayer adsorption, and the adsorption sites on the Ag–Cu–CeO_2 nanocomposites are heterogeneous. When 'n', the exponent in the Freundlich equation, is greater than 1, it suggests a favorable adsorption process [51].

The obtained values of 'B' and 'E' from the Dubinin-Radushkevich (D-R) isotherm analysis suggest that the adsorption behavior of the nanocomposites is influenced by both physical and chemical forces. Moreover, the activation energy for adsorption is found to be composition-dependent, indicating that it varies based on the specific composition of the nanocomposite material [54].

6. Thermodynamic parameters

The thermodynamic parameters were analyzed to confirm the addition of energy and transfer of ions taking place during the removal of CR dye at various temperatures. Table 5 summarizes the thermodynamic parameter for the CR adsorption onto Ag–Cu–CeO_2 nanocomposites. The determination of ΔH^0 (standard entropy change) and ΔS^0 (standard enthalpy change) involves estimating these values from the intercept and slope of the ΔG0 versus temperature curve, as depicted in Fig. 14.

CR is thought to slowly bind as the temperature rises because negative values of (ΔH^0) and (ΔS^0) imply an exothermic sorption process and a reduction in randomness in the adsorption process, respectively [55]. Additionally, as the temperature rises, the value of (ΔG^0) rises, which suggests that lower temperature makes the adsorption more favorable. These results suggest that the CR adsorption is thermodynamically viable, and the exothermic nature of the process suggests heat is released during adsorption [56]However, the reduction in randomness during the process of adsorption implies that increasing temperature leads to slower binding of CR to the adsorbents [57].

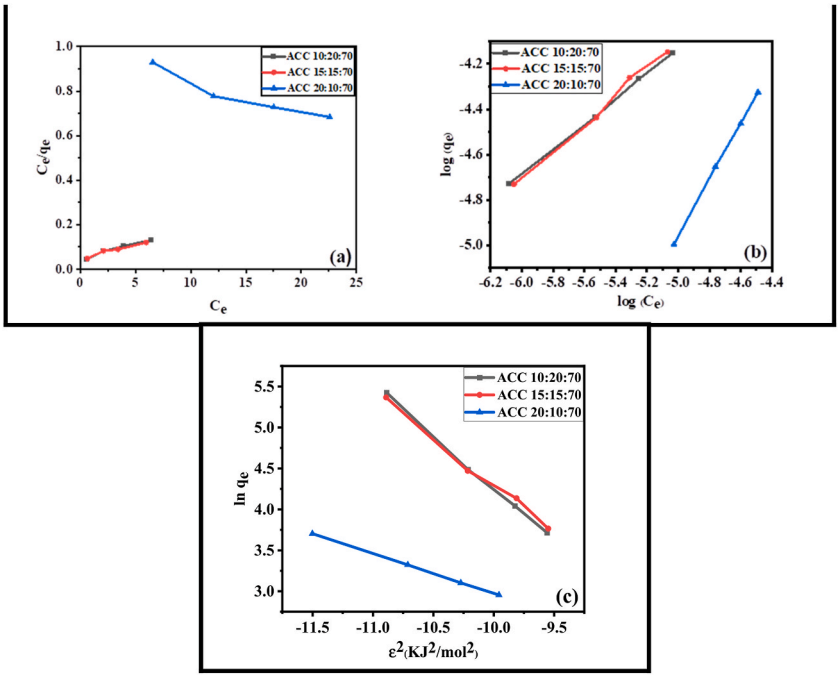

Fig. 13. (a) Langmuir Isotherm (b) Freundlich isotherm (c) D-R isotherm for adsorption of Congo Red on Ag–Cu–CeO_2 (Temperature - 20 °C, C_o - 55.6 mgl^{-1}, m - 0.1 g, pH- 2 and Time- 180 min).

Table 4
Isotherm constants for adsorption of Congo Red by Ag–Cu–CeO_2 nanocomposites.

	R_L^2	K_L	q_{max} (mg/g)	R_F^2	K_F (mg/g)	n	R^2	B_D mol^2/Kj	E Kj/mol
ACC 10:20:70	0.9629	0.329	69.93	0.9994	3.471	1.81	0.9979	1.285	0.623
ACC 15:15:70	0.9512	0.277	78.12	0.9937	3.437	1.65	0.9927 1	167	0.654
ACC 20:10:70	0.9097	0.014	67.56	0.9996	1.179	0.80	0.9999	0.487	1.013

Table 5
Thermodynamic constants for adsorption of Congo Red by Ag–Cu–CeO_2 nanocomposites.

Nanocomposite	ΔH^o ($kJmol^{-1}$)	ΔS^o ($kJmol^{-1}$)	ΔG^0 ($kJmol^{-1}$) 283 K	293K	293K	303K	313K	323K	R^2 333 K
ACC 10:20:70	−27.573	−0.072	−0.50	−0.40	−0.34	−0.29	−0.25	−0.21	0.9823
ACC 15:15:70	−26.431	−0.069	−0.51	−0.40	−0.34	−0.31	−0.25	−0.19	0.9796
ACC 20:10:70	−16.637	−0.052	−0.13	−0.08	−0.05	−0.01	0.01	0.05	0.9974

7. Kinetics studies

The pseudo-first-order (PFO) and pseudo-second-order (PSO) models were used to characterise the CR's adsorption kinetics onto the Ag–Cu–CeO_2 nanocomposites adsorbent surfaces. The dynamic parameters of the adsorption process were established by utilizing the slopes and intercepts of the plots presented in Fig. 15 (a) (1st-order kinetics model) and Fig. 15 (b) (2nd-order kinetic model). The values obtained from both models were recorded in Table 6. The study revealed notable differences in the R^2 values between the pseudo-second-order (PSO) models and the pseudo-first-order (PFO) models. Specifically, it was found that the PSO models' R^2 values were higher (0.9959, 0.9963, and 0.9903) than the PFO models' (0.9806, 0.9352, and 0.9252, respectively) for the ACC 10:20:70, ACC 15:15:70, and ACC 20:10:70 compositions. In light of this, the Ag–Cu–CeO_2 nanocomposites adsorbent was governed by the PSO model [58]. The Pseudo-Second-Order adsorption mechanism is characterized by a chemical process where the adsorption rate is regulated by the sharing of electrons. This mechanism suggests that covalent forces play a crucial role in the adsorption process, resulting in a stronger interaction between the adsorbent and adsorbate [13,59]. Furthermore, the comparison between the calculated values of q_e ($q_{e\ calc'}$) obtained from the slopes of the second-order plots and the experimental values of q_e ($q_{e\ exp}$) revealed a high degree of

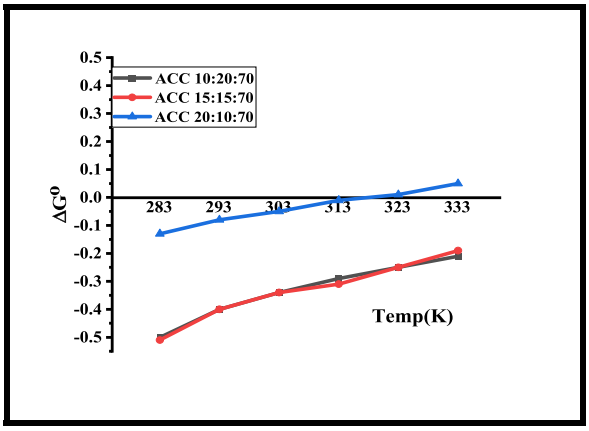

Fig. 14. Thermodynamic study of removal of Congo Red. Temperature – 20–60 °C(283–333K), Co - 55.6 mgl−1, m - 0.1 g, pH- 2 and Time- 180 min).

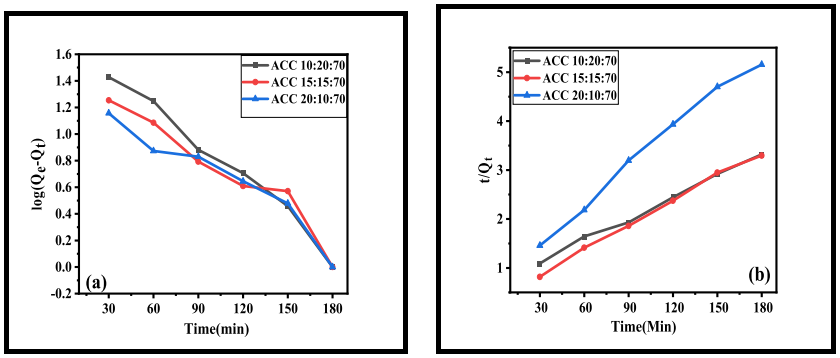

Fig. 15. (a) Pseudo First Order Kinetics. (b) Pseudo Second Order Kinetics plot for adsorption of Congo Red by Ag–Cu–CeO_2 nanocomposites (Initial concentration-55.6 mg/l, pH-2, m-0.1g, Temp- 20 °C, Time- 180 min).

Table 6
Parameters of the First- and Second-order kinetic models for adsorption of Congo Red by Ag–Cu–CeO_2 nanocomposite.

	First Order				Second Order			
Nanocomposite	q_e *exp*	$q_e calc'$	k_1	R^2	q_e *exp*	$q_e calc'$	k_1	R^2
ACC 10:20:70	54.22	0.172	0.021	0.9806	54.22	68.02	$3*10^{-4}$	0.9959
ACC 15:15:70	54.58	0.218	0.021	0.9352	54.58	59.88	$7*10^{-4}$	0.9963
ACC 20:10:70	34.91	0.251	0.015	0.9255	34.91	39.21	$8*10^{-4}$	0.9903

similarity. This observation suggests that the pseudo-Second-order kinetic model is well-suited for accurately representing the empirical data of this adsorption process.

8. Desorption and reusability studies

In the course of investigating the desorption of CR, a batch adsorption process was employed using different reagents. Results obtained indicate NaOH was the optimum choice for desorption of CR. The adsorption process was allowed to reach equilibrium, and then the adsorbent was centrifuged to separate it and rinsed with deionized water. Subsequently, the adsorbent was placed in a conical flask containing the desorbing agent and permitted to stay at room temperature for 24 h [60] The study revealed that the maximal CR dye desorption was achieved using a 0.1 M NaOH solution, with an 82 % removal rate recorded.

In order to test the reusability of nanocomposites, a series of cycles of adsorption were performed. The recycling test was performed specifically on the ACC 15:15:70 nanocomposite, which gives the best adsorption results among the three nanocomposites tested during the batch adsorption experiment.

The stability of the CR removing capacity of the ACC 15:15:70 nanocomposite was studied and presented in Fig. 16. The results revealed that the removal capacity remained highly stable over multiple cycles, indicating no significant loss in activity. The

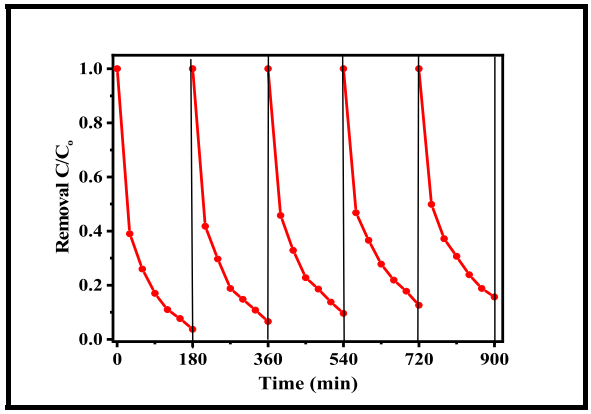

Fig-16. Cycling runs of Removal of Congo Red by using ACC 15:15:70 nanocomposite.

nanocomposite demonstrated less than 12 % deactivation after five cycles of use, which is a promising indication of its durability and reliability in removing CR.

9. Adsorption mechanism

The Inclusion of metal ions (Ce^{3+}, Cu^{2+}, and Ag^{+}) results in positively charged surface sites in the Ag–Cu–CeO_2 nanocomposite. CR, being negatively charged, is electrostatically attracted to the positively charged surface [61]. This initial interaction permits the dye molecules to approach the surface of the nanocomposite [62]. Additionally, the presence of hydrogen bonding between the nanocomposite surface and CR is also evident. The hydroxyl groups on the nanocomposite surface establish hydrogen bonds with the CR sulfonic acid groups and other functional groups [63] Fig. 17. Furthermore, the Ce–O and Cu–O bonds may participate in the formation of coordination complexes with CR, enhancing its adsorption. The hypothesised adsorption mechanism involves a combination of electrostatic interactions, hydrogen bonding, and coordination complex formation. These interactions all lead to the adsorption of CR onto the Ag–Cu–CeO_2 nanocomposite surface. The FT-IR analysis data support this mechanism by offering insights into the individual bonds and interactions involved in the adsorption process.

In Table 7, Distinct adsorbents utilized for the adsorption of CR are compared with the removal capability of Metal Mixed Oxide Nanomaterials, as well as their methods of manufacture. Ag–Cu–CeO_2, as shown in table, offers itself as a promising and effective adsorbent for colour removal of CR dye from polluted water.

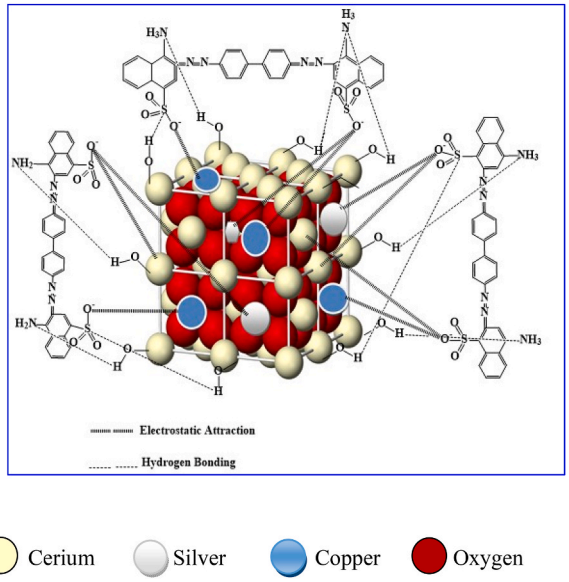

Fig. 17. Illustration of the possible interaction between nanocomposites and Congo red including electrostatic forces and hydrogen bonding.

Table 7
Comparison of the Synthesis Route and removal capacity of different metal oxide nanocomposites adsorbent toward Congo Red dye.

Material	Synthesis Route	Removal capacity	References
Fe_2O_3–MgO Nanocomposite	One step hydrothermal method	95 %	[64]
$Fe_xCo_{3-x}O_4$ Nanoparticles	Aqueous Precipitation Method	86.12 %	[65]
CeB_4 Nanocrystal	Molten salt method	97.8 %	[66]
Fe_3O_4@carbon@ZIF-8 Nanoparticles	Self-assembly	~80 %	[67]
Polyaniline-zinc titanate nanocomposite	Polymerisation reaction	98 %	[68]
L-cysteine decorated rGO/Polyaniline	Aqueous Precipitation	98 %	[69]
Biosynthesized ZnO Nanoparticles	Sol-gel technique.	92 %	[70]
ZnO/Chitosan Nanocomposites	In-situ Precipitation	90 %	[71]
Biosynthesized ZnO Nanoparticles	Green Synthesis	94.125 %	[72]
Fe_3O_4-TSPED- Tryptophan nanoparticles	Simple Precipitation Method	99 %	[73]
Ag–Cu–CeO_2 nanocomposites	Aqueous Co-precipitation method	96.83 %	This Study

10. Conclusion

In this study, the Ag–Cu–CeO_2 nanocomposites synthesized by facile aqueous coprecipitation method had fluorite structure with crystallite size in the range 6.00–6.87 nm and particles in the range of 5.5 ± 1 nm The synthesized Ag–Cu–CeO_2 nanocomposites were explored for their potential as adsorbents for the elimination of CR from water. Our findings demonstrate that the nanocomposites are highly effective adsorbents with significant potential for use in water treatment applications. Through the use of various Characterization techniques, we were able to thoroughly investigate the nanocomposites. Our analysis revealed that the nanocomposites showed higher adsorption rates at pH values of 2 for all three compositions: Ag–Cu–CeO_2 10:20:70, Ag–Cu–CeO_2 15:15:70, and Ag–Cu–CeO_2 20:10:70. The maximum removal of CR dye was 53.93, 54.71, and 37.80 mg/g for each composition, respectively, using an optimal adsorbent dose of 0.1 g and temperature of 20 °C. We also found that maximum adsorption was achieved at an equilibrium time of 180 min.

The data were best suited by the Freundlich adsorption isotherm and pseudo-second-order kinetic model, with high R^2 values for each composition, demonstrating the effectiveness of the nanocomposites in removing CR dye. Furthermore, the negative values of enthalpy variation (−27.57, −26.43, and −16.73 kJ/mol) demonstrated that the adsorption was spontaneous and exothermic. The enhanced surface functionalities of the Ag–Cu–CeO_2 nanocomposites serve for the adsorption mechanism for CR. In essence, electrostatic attraction, co-ordination complex formation and interactions involving hydrogen bonds are both substantial contributors to this adsorption mechanism. In conclusion, our findings demonstrate that Ag–Cu–CeO_2 nanocomposites hold significant potential as effective and environment-friendly adsorbents for CR removal from water. These nanocomposites have the potential to be used as an effective remedy towards dye pollution and wastewater treatment.

Data availability statement

Data associated with this study has not been deposited into a publicly available repository. Data will be made available on request.

CRediT authorship contribution statement

Nitish Semwal: Data curation, Investigation. **Divya Mahar:** Data curation. **Manjunath Chatti:** Software, Validation, Writing – review & editing. **Anirban Dandapat:** Writing – review & editing. **Mahesh Chandra Arya:** Conceptualization, Resources, Writing – original draft, Writing – review & editing.

Declaration of competing interest

The authors declare that they have no known competing financial interests or personal relationships that could have appeared to influence the work reported in this paper.

References

[1] M.A. Nistor, S.G. Muntean, R. Ianoș, R. Racoviceanu, C. Ianași, L. Cseh, Adsorption of anionic dyes from wastewater onto magnetic nanocomposite powders synthesized by combustion method, Appl. Sci. 11 (19) (2021, October 4) 9236, https://doi.org/10.3390/app11199236.
[2] W.A. Shaikh, S. Chakraborty, R.U. Islam, A.A. Ghfar, M. Naushad, J. Bundschuh, J.P. Maity, N.K. Mondal, Fabrication of biochar-based hybrid Ag nanocomposite from algal biomass waste for toxic dye-laden wastewater treatment, Chemosphere 289 (2022), 133243, https://doi.org/10.1016/j.chemosphere.2021.133243.
[3] A.H. Jawad, A.S. Abdulhameed, Mesoporous Iraqi red kaolin clay as an efficient adsorbent for methylene blue dye: adsorption kinetic, isotherm and mechanism study, Surface. Interfac. 18 (2020), 100422, https://doi.org/10.1016/j.surfin.2019.100422.
[4] S.R. Ali, R. Kumar, S.K. Kadabinakatti, M.C. Arya, Enhanced UV and visible light—driven photocatalytic degradation of tartrazine by nickel-doped cerium oxide nanoparticles, Mater. Res. Express 6 (2018), 025513, https://doi.org/10.1088/2053-1591/aaee44.
[5] K. Rosli, A.S. Abdulhameed, S.N. Surip, Z.A. Alothman, A.H. Jawad, An eco-friendly adsorbent of chitosan/montmorillonite/algae for removal of basic green 1 and reactive blue 19 dyes: box-behnken design optimization mechanistic study, J. Polym. Environ. 31 (2023) 3907–3924, https://doi.org/10.1007/s10924-023-02869-z.

[6] G. Murugadoss, D.D. Kumar, M.R. Kumar, N. Venkatesh, P. Sakthivel, Silver decorated CeO2 nanoparticles for rapid photocatalytic degradation of textile rose bengal dye, Sci. Rep. 11 (2021), https://doi.org/10.1038/s41598-020-79993-6.

[7] R. Al-Tohamy, S.S. Ali, F. Li, K.M. Okasha, Y.A.-G. Mahmoud, T. Elsamahy, H. Jiao, Y. Fu, J. Sun, A critical review on the treatment of dye-containing wastewater: ecotoxicological and health concerns of textile dyes and possible remediation approaches for environmental safety, Ecotoxicol. Environ. Saf. 231 (2022), 113160, https://doi.org/10.1016/j.ecoenv.2021.113160.

[8] N.A. Alamrani, H.A. AL-Aoh, Elimination of Congo red dye from industrial wastewater using teucrium polium L. As a low-cost local adsorbent, Adsorption Science & Technology 2021 (2021) 1–12, https://doi.org/10.1155/2021/5728696.

[9] N.I. Normi, A.S. Abdulhameed, A.H. Jawad, S.N. Surip, R. Razuan, M.L. Ibrahim, Hydrothermal-Assisted grafting of schiff base chitosan by salicylaldehyde for adsorptive removal of acidic dye: statistical modeling and adsorption mechanism, J. Polym. Environ. 31 (2022) 1925–1937, https://doi.org/10.1007/s10924-022-02730-9.

[10] A. Afkhami, R. Moosavi, Adsorptive removal of Congo red, a carcinogenic textile dye, from aqueous solutions by maghemite nanoparticles, J. Hazard Mater. 174 (2010) 398–403, https://doi.org/10.1016/j.jhazmat.2009.09.066.

[11] N.K. Soliman, A.F. Moustafa, H.R.A. El-Mageed, O.F. Abdel-Gawad, E.T. Elkady, S.A. Ahmed, H.S. Mohamed, Experimentally and theoretically approaches for disperse red 60 dye adsorption on novel quaternary nanocomposites, Sci. Rep. 11 (2021), https://doi.org/10.1038/s41598-021-89351-9.

[12] S. Gao, W. Zhang, Z. An, S. Kong, D. Chen, Adsorption of anionic dye onto magnetic Fe3O4/CeO2 nanocomposite: equilibrium, kinetics, and thermodynamics, Adsorpt. Sci. Technol. 37 (2019) 185–204, https://doi.org/10.1177/0263617418819164.

[13] E. Nyankson, J. Adjasoo, J.K. Efavi, A. Yaya, G. Manu, A. Kingsford, R.Y. Abrokwah, Synthesis and kinetic adsorption characteristics of Zeolite/CeO2 nanocomposite, Scientific African 7 (2020), e00257, https://doi.org/10.1016/j.sciaf.2019.e00257.

[14] T.A. Alrebdi, H.A. Ahmed, S.H. Alrefaee, R.A. Pashameah, A. Toghan, A.M. Mostafa, F.H. Alkallas, A. Rezk, R, Enhanced adsorption removal of phosphate from water by Ag-doped PVA-NiO nanocomposite prepared by pulsed laser ablation method, J. Mater. Res. Technol. 20 (2022) 4356–4364, https://doi.org/10.1016/j.jmrt.2022.08.165.

[15] S.K. Pradhan, J. Panwar, S. Gupta, Enhanced heavy metal removal using silver-yttrium oxide nanocomposites as novel adsorbent system, J. Environ. Chem. Eng. 5 (2017) 5801–5814, https://doi.org/10.1016/j.jece.2017.11.007.

[16] F. Ostovar, R. Ansari, H.J.G.N.J. Moafi, Preparation and application of silver oxide/sawdust nanocomposite for Chromium (VI) ion removal from aqueous solutions using column system (2017), Issue 3 19 (2022) 412–422, https://doi.org/10.30955/gnj.002225.

[17] L. Taneja, S. Raghav, C. Kochar, P.K. Yadav, S. Swarupa Tripathy, Effective remediation of fluoride from drinking water using cerium-silver oxide composite incorporated with reduced graphene oxide, J. Water Process Eng. 44 (2021), 102369, https://doi.org/10.1016/j.jwpe.2021.102369.

[18] A. Ahmad, S. Hamidah Mohd Setapar, A. Ali Yaqoob, M. Nasir Mohamad Ibrahim, Synthesis and characterization of GO-Ag nanocomposite for removal of malachite dye from aqueous solution, Mater. Today: Proc. 47 (2021) 1359–1365, https://doi.org/10.1016/j.matpr.2021.03.643.

[19] A.A. Olajire, L.A. Bamigbade, Green synthesis of chitosan-based iron@silver nanocomposite as adsorbent for wastewater treatment, Water Resour. Ind. 26 (2021), 100158, https://doi.org/10.1016/j.wri.2021.100158.

[20] N. Ayawei, A.N. Ebelegi, D. Wankasi, Modelling and interpretation of adsorption isotherms, Journal of Chemistry 2017 (2017) 1–11, https://doi.org/10.1155/2017/3039817.

[21] S. Kalam, S.A. Abu-Khamsin, M.S. Kamal, S. Patil, Surfactant adsorption isotherms: a review, ACS Omega 6 (2021) 32342–32348, https://doi.org/10.1021/acsomega.1c04661.

[22] N.N. Bahrudin, M.A. Nawi, A.H. Jawad, S. Sabar, Adsorption characteristics and mechanistic study of immobilized chitosan-montmorillonite composite for methyl orange removal, J. Polym. Environ. 28 (2020) 1901–1913, https://doi.org/10.1007/s10924-020-01734-7.

[23] A.H. Jawad, A.S. Abdulhameed, E. Kashi, Z.M. Yaseen, Z.A. Alothman, M.R. Khan, Cross-linked chitosan-glyoxal/kaolin clay composite: parametric optimization for color removal and COD reduction of remazol brilliant blue R dye, J. Polym. Environ. 30 (2021) 164–178, https://doi.org/10.1007/s10924-021-02188-1.

[24] A.H. Jawad, A.S. Abdulhameed, N.N.A. Malek, Z.A. Alothman, Statistical optimization and modeling for color removal and COD reduction of reactive blue 19 dye by mesoporous chitosan-epichlorohydrin/kaolin clay composite, Int. J. Biol. Macromol. 164 (2020) 4218–4230, https://doi.org/10.1016/j.ijbiomac.2020.08.201.

[25] Y. Dong, K. Wang, Y. Tan, Q. Wang, J. Li, H. Mark, S. Zhang, Synthesis and characterization of pure copper nanostructures using wood inherent architecture as a natural template, Nanoscale Res. Lett. 13 (2018), https://doi.org/10.1186/s11671-018-2543-0.

[26] A.K. Sasmal, S. Dutta, T. Pal, A ternary Cu2O–Cu–CuO nanocomposite: a catalyst with intriguing activity, Dalton Trans. 45 (2016) 3139–3150, https://doi.org/10.1039/c5dt03859f.

[27] N. Lam, R. Smith, N. Le, C. Thuy, M. Tamboli, A. Tamboli, S. Alshehri, M. Ghoneim, N. Truong, J. Jung, Evaluation of the structural deviation of Cu/Cu2O nanocomposite using the X-ray diffraction analysis methods, Crystals 12 (2022) 566, https://doi.org/10.3390/cryst12040566.

[28] M.M. Khan, S.A. Ansari, J.-H. Lee, M.O. Ansari, J. Lee, M.H. Cho, Electrochemically active biofilm assisted synthesis of Ag@CeO2 nanocomposites for antimicrobial activity, photocatalysis and photoelectrodes, J. Colloid Interface Sci. 431 (2014) 255–263, https://doi.org/10.1016/j.jcis.2014.06.026.

[29] S.V. Kumar, A.P. Bafana, P. Pawar, A. Rahman, S.A. Dahoumane, C.S. Jeffryes, High conversion synthesis of <10 nm starch-stabilized silver nanoparticles using microwave technology, Sci. Rep. 8 (2018), https://doi.org/10.1038/s41598-018-23480-6.

[30] M.A. Salam, S.S. Al-Juaid, A.H. Qusti, A.A. Hermas, Electrochemical deposition of a carbon nanotube-poly(o-phenylenediamine) composite on a stainless steel surface, Synth. Met. 161 (2011) 153–157, https://doi.org/10.1016/j.synthmet.2010.11.014.

[31] S. Guan, Q. Huang, J. Ma, W. Li, A.T. Ogunbiyi, Z. Zhou, K. Chen, Q. Zhang, HCHO removal by MnO2(x)–CeO2: influence of the synergistic effect on the catalytic activity, Ind. Eng. Chem. Res. 59 (2019) 596–608, https://doi.org/10.1021/acs.iecr.9b05191.

[32] S.A.R. Hashmi, H.C. Prasad, R. Abishera, H.N. Bhargaw, A. Naik, Improved recovery stress in multi-walled-carbon-nanotubes reinforced polyurethane, Mater. Des. 67 (2015) 492–500, https://doi.org/10.1016/j.matdes.2014.10.062.

[33] R. Ahmad, K. Ansari, Comparative study for adsorption of Congo red and methylene blue dye on chitosan modified hybrid nanocomposite, Process Biochem. 108 (2021) 90–102, https://doi.org/10.1016/j.procbio.2021.05.013.

[34] N. Nagarjun, M. Jacob, P. Varalakshmi, A. Dhakshinamoorthy, UiO-66(Ce) metal-organic framework as a highly active and selective catalyst for the aerobic oxidation of benzyl amines, Mol. Catal. 499 (2021), 111277, https://doi.org/10.1016/j.mcat.2020.111277.

[35] P.P. Kannan, N.K. Karthick, G. Arivazhagan, Hydrogen bond interactions in the binary solutions of formamide with methanol: FTIR spectroscopic and theoretical studies, Spectrochim. Acta Mol. Biomol. Spectrosc. 229 (2020), 117892, https://doi.org/10.1016/j.saa.2019.117892.

[36] J.S. Binoj, M. Jaafar, B.B. Mansingh, A.K. Pulikkal, Comprehensive investigation of Areca catechu tree peduncle biofiber reinforced biocomposites: influence of fiber loading and surface modification, Biomass Conversion and Biorefinery (2023), https://doi.org/10.1007/s13399-023-04182-0.

[37] G. Murugadoss, K. Thiruppathi, N. Venkatesh, S. Hazra, A. Mohankumar, G. Thiruppathi, M.R. Kumar, P. Sundararaj, J.R. Rajabathar, P. Sakthivel, Construction of novel quaternary nanocomposite and its synergistic effect towards superior photocatalytic and antibacterial application, J. Environ. Chem. Eng. 10 (2022), 106961, https://doi.org/10.1016/j.jece.2021.106961.

[38] W. Xie, F. Yao, H. Gu, A. Du, Q. Lei, N. Naik, Z. Guo, Magnetoresistive and Piezoresistive Polyaniline Nanoarrays In-Situ Polymerized Surrounding Magnetic Graphene Aerogel. Advanced Composites and Hybrid Materials 5, 2022, pp. 1003–1016, https://doi.org/10.1007/s42114-021-00413-y.

[39] T. Ivanova, A. Harizanova, T. Koutzarova, B. Vertruyen, Sol–gel Nanocrystalline ZnO:Ag Films: Structural and Optical Properties. Superlattices and Microstructures 70, 2014, pp. 1–6, https://doi.org/10.1016/j.spmi.2014.03.007.

[40] V. Thiruvengadam, A.V.J.B.R.A.C. Bansod, Characterization of silver nanoparticles synthesized using chemical method and its antibacterial property, Biointerface Research in Applied Chemistry 10 (2020) 7257–7264, https://doi.org/10.33263/briac106.72577264.

[41] S. Yasmeen, M. Kabiraz, B. Saha, Md Qadir, Md Gafur, S. Masum, Chromium (VI) ions removal from tannery effluent using chitosan-microcrystalline cellulose composite as adsorbent, Int. Res. J. Pure Appl. Chem. 10 (2016) 1–14, https://doi.org/10.9734/irjpac/2016/23315.

[42] J. Hedberg, E. Blomberg, I. Odnevall Wallinder, In the search for nanospecific effects of dissolution of metallic nanoparticles at freshwater-like conditions: a critical review, Environ. Sci. Technol. 53 (2019) 4030–4044, https://doi.org/10.1021/acs.est.8b05012.

[43] A. Sabir, T.A. Sherazi, Q. Xu, Porous polymer supported Ag-TiO2 as green photocatalyst for degradation of methyl orange, Surface. Interfac. 26 (2021), 101318, https://doi.org/10.1016/j.surfin.2021.101318.

[44] A.H. Jawad, A.S. Abdulhameed, M.S. Mastuli, Mesoporous crosslinked chitosan-activated charcoal composite for the removal of thionine cationic dye: comprehensive adsorption and mechanism study, J. Polym. Environ. 28 (2020) 1095–1105, https://doi.org/10.1007/s10924-020-01671-5.

[45] A.H. Jawad, A.S. Abdulhameed, L.D. Wilson, M.A.K.M. Hanafiah, W.I. Nawawi, Z.A. Alothman, M. Rizwan Khan, Fabrication of schiff's base chitosan-glutaraldehyde/activated charcoal composite for cationic dye removal: optimization using response surface methodology, J. Polym. Environ. 29 (2021) 2855–2868, https://doi.org/10.1007/s10924-021-02057-x.

[46] F. Ambroz, T.J. Macdonald, V. Martis, I.P. Parkin, Evaluation of the BET theory for the characterization of meso and microporous MOFs, Small Methods 2 (2018), 1800173, https://doi.org/10.1002/smtd.201800173.

[47] S. Banerjee, M.C. Chattopadhyaya, Adsorption characteristics for the removal of a toxic dye, tartrazine from aqueous solutions by a low cost agricultural by-product, Arab. J. Chem. 10 (2017) S1629–S1638, https://doi.org/10.1016/j.arabjc.2013.06.005.

[48] J. Kaur, S. Bhukal, K. Gupta, M. Tripathy, S. Bansal, S. Singhal, Nanocomposite of CeO 2 and ZnO: an active material for the treatment of contaminated water, Mater. Chem. Phys. 177 (2016) 512–520, https://doi.org/10.1016/j.matchemphys.2016.04.063.

[49] J. Abdi, M. Vossoughi, N.M. Mahmoodi, I. Alemzadeh, Synthesis of metal-organic framework hybrid nanocomposites based on GO and CNT with high adsorption capacity for dye removal, Chem. Eng. J. 326 (2017) 1145–1158, https://doi.org/10.1016/j.cej.2017.06.054.

[50] S. Noreen, M. Tahira, M. Ghamkhar, I. Hafiz, H.N. Bhatti, R. Nadeem, M.A. Murtaza, M. Yaseen, A.A. Sheikh, Z. Naseem, et al., Treatment of textile wastewater containing acid dye using novel polymeric graphene oxide nanocomposites (GO/PAN,GO/PPy, GO/PSty), J. Mater. Res. Technol. 14 (2021) 25–35, https://doi.org/10.1016/j.jmrt.2021.06.007.

[51] M.A. Al-Ghouti, R.S. Al-Absi, Mechanistic understanding of the adsorption and thermodynamic aspects of cationic methylene blue dye onto cellulosic olive stones biomass from wastewater, Sci. Rep. 10 (2020), https://doi.org/10.1038/s41598-020-72996-3.

[52] S. Mondal, K. Aikat, G. Halder, Biosorptive uptake of ibuprofen by chemically modified Parthenium hysterophorus derived biochar: equilibrium, kinetics, thermodynamics and modeling, Ecol. Eng. 92 (2016) 158–172, https://doi.org/10.1016/j.ecoleng.2016.03.022.

[53] A.H. Jawad, S.E.M. Saber, A.S. Abdulhameed, A.M. Farhan, Z.A. Alothman, L.D. Wilson, Characterization and applicability of the natural Iraqi bentonite clay for toxic cationic dye removal: adsorption kinetic and isotherm study, J. King Saud Univ. Sci. 35 (2023), 102630, https://doi.org/10.1016/j.jksus.2023.102630.

[54] A. Khadir, M. Negarestani, A. Mollahosseini, Sequestration of a non-steroidal anti-inflammatory drug from aquatic media by lignocellulosic material (Luffa cylindrica) reinforced with polypyrrole: study of parameters, kinetics, and equilibrium, J. Environ. Chem. Eng. 8 (2020), 103734, https://doi.org/10.1016/j.jece.2020.103734.

[55] H. Shayesteh, A. Rahbar-Kelishami, R. Norouzbeigi, Evaluation of natural and cationic surfactant modified pumice for Congo red removal in batch mode: kinetic, equilibrium, and thermodynamic studies, J. Mol. Liq. 221 (2016) 1–11, https://doi.org/10.1016/j.molliq.2016.05.053.

[56] J.H. Potgieter, C. Pardesi, S. Pearson, A kinetic and thermodynamic investigation into the removal of methyl orange from wastewater utilizing fly ash in different process configurations, Environ. Geochem. Health 43 (2020) 2539–2550, https://doi.org/10.1007/s10653-020-00567-6.

[57] P. Chakraborty, S. Show, S. Banerjee, G. Halder, Mechanistic insight into sorptive elimination of ibuprofen employing bi-directional activated biochar from sugarcane bagasse: performance evaluation and cost estimation, J. Environ. Chem. Eng. 6 (2018) 5287–5300, https://doi.org/10.1016/j.jece.2018.08.017.

[58] P. Koohi, A. Rahbar-kelishami, H. Shayesteh, Efficient removal of Congo red dye using Fe3O4/NiO nanocomposite: synthesis and characterization, Environ. Technol. Innovat. 23 (2021), 101559, https://doi.org/10.1016/j.eti.2021.101559.

[59] N. Beigi, H. Shayesteh, S. Javanshir, M. Hosseinzadeh, Pyrolyzed magnetic NiO/carbon-derived nanocomposite from a hierarchical nickel-based metal-organic framework with ultrahigh adsorption capacity, Environ. Res. 231 (2023), 116146, https://doi.org/10.1016/j.envres.2023.116146.

[60] G. Murambasvina, C. Mahamadi, Effective Fluoride Adsorption Using Water Hyacinth Beads Doped with Hydrous Oxides of Aluminium and Iron, Groundwater for Sustainable Development 10, 2020, 100302, https://doi.org/10.1016/j.gsd.2019.100302.

[61] A.H. Jawad, A. Saud Abdulhameed, L.D. Wilson, S.S.A. Syed-Hassan, Z.A. Alothman, M. Rizwan Khan, High surface area and mesoporous activated carbon from KOH-activated dragon fruit peels for methylene blue dye adsorption: optimization and mechanism study, Chin. J. Chem. Eng. 32 (2021) 281–290, https://doi.org/10.1016/j.cjche.2020.09.070.

[62] A.S. Abdulhameed, N.N.M. Firdaus Hum, S. Rangabhashiyam, A.H. Jawad, L.D. Wilson, Z.M. Yaseen, A.A. Al-Kahtani, Z.A. Alothman, Statistical modeling and mechanistic pathway for methylene blue dye removal by high surface area and mesoporous grass-based activated carbon using K2CO3 activator, J. Environ. Chem. Eng. 9 (2021), 105530, https://doi.org/10.1016/j.jece.2021.105530.

[63] A.H. Jawad, A.S. Abdulhameed, Facile synthesis of crosslinked chitosan-tripolyphosphate/kaolin clay composite for decolourization and COD reduction of remazol brilliant blue R dye: optimization by using response surface methodology, Colloids Surf. A Physicochem. Eng. Asp. 605 (2020), 125329, https://doi.org/10.1016/j.colsurfa.2020.125329.

[64] S.K. Sahoo, J.P. Dhal, G.K. Panigrahi, Magnesium oxide nanoparticles decorated iron oxide nanorods: synthesis, characterization and remediation of Congo red dye from aqueous media, Compos. Commun. 22 (2020), 100496, https://doi.org/10.1016/j.coco.2020.100496.

[65] J. Liu, N. Wang, H. Zhang, J. Baeyens, Adsorption of Congo red dye on FexCo3-xO4 nanoparticles, J. Environ. Manag. 238 (2019) 473–483, https://doi.org/10.1016/j.jenvman.2019.03.009.

[66] C. Wang, Y. Li, R. Shen, X. Liu, Cerium tetraboride synthesized by a molten salt method and its Congo red adsorption performance, Adv. Powder Technol. (2021), https://doi.org/10.1016/j.apt.2021.04.029.

[67] Z. Xiong, H. Zheng, Y. Hu, X. Hu, W. Ding, J. Ma, Y. Li, Selective adsorption of Congo red and Cu(II) from complex wastewater by core-shell structured magnetic carbon@zeolitic imidazolate frameworks-8 nanocomposites, Sep. Purif. Technol. 277 (2021), 119053, https://doi.org/10.1016/j.seppur.2021.119053.

[68] S. Singh, S. Perween, A. Ranjan, Dramatic enhancement in adsorption of Congo red dye in polymer-nanoparticle composite of polyaniline-zinc titanate, J. Environ. Chem. Eng. 9 (2021), 105149, https://doi.org/10.1016/j.jece.2021.105149.

[69] S. Razzaq, M. Akhtar, S. Zulfiqar, S. Zafar, I. Shakir, P.O. Agboola, S. Haider, M.F. Warsi, Adsorption removal of Congo red onto L-cysteine/rGO/PANI nanocomposite: equilibrium, kinetics and thermodynamic studies, J. Taibah Univ. Sci. 15 (2021) 50–62, https://doi.org/10.1080/16583655.2021.1876351.

[70] P. Palai, S. Muduli, B. Priyadarshini, T.R. Sahoo, A facile green synthesis of ZnO nanoparticles and its adsorptive removal of Congo red dye from aqueous solution, Mater. Today: Proc. 38 (2021) 2445–2451, https://doi.org/10.1016/j.matpr.2020.07.387.

[71] N.T. Nguyen, N.T. Nguyen, V.A. Nguyen, In situ synthesis and characterization of ZnO/chitosan nanocomposite as an adsorbent for removal of Congo red from aqueous solution, Adv. Polym. Technol. 2020 (2020) 1–8, https://doi.org/10.1155/2020/3892694.

[72] P. Debnath, N.K. Mondal, Effective removal of Congo red dye from aqueous solution using biosynthesized zinc oxide nanoparticles, Environ. Nanotechnol. Monit. Manag. 14 (2020), 100320, https://doi.org/10.1016/j.enmm.2020.100320.

[73] J.K. Sahoo, S.K. Paikra, M. Mishra, H. Sahoo, Amine functionalized magnetic iron oxide nanoparticles: synthesis, antibacterial activity and rapid removal of Congo red dye, J. Mol. Liq. 282 (2019) 428–440, https://doi.org/10.1016/j.molliq.2019.03.033.